

Modulating the electronic spin state by constructing dual-metal atomic pairs for activating the dynamic site of oxygen reduction reaction

Shenghua Ye^{1,3,§}, Shuhua Xie^{1,§}, Yaqi Lei^{1,§}, Xiuyuan Yang¹, Jing Hu¹, Lirong Zheng⁴, Zhida Chen¹, Yonghuan Fu¹, Xiangzhong Ren¹, Yongliang Li¹, Xiaoping Ouyang⁵, Qianling Zhang¹ (✉), Jianhong Liu^{1,3} (✉), and Xueliang Sun² (✉)

¹ College of Chemistry and Environmental Engineering, Graphene Composite Research Center, Shenzhen University, Shenzhen 518060, China

² Department of Mechanical and Materials Engineering, University of Western Ontario, London, Ontario N6A 5B9, Canada

³ Shenzhen Eigen-Equation Graphene Technology Co. Ltd., Shenzhen 518000, China

⁴ Institute of High Energy Physics Chinese Academy of Sciences, Beijing 100049, China

⁵ School of Materials Science and Engineering, Xiangtan University, Xiangtan 411105, China

[§] Shenghua Ye, Shuhua Xie, and Yaqi Lei contributed equally to this work.

© Tsinghua University Press 2022

Received: 5 August 2022 / Revised: 26 August 2022 / Accepted: 27 August 2022

ABSTRACT

In this study, dual-metal atomic pairs of manganese (Mn)-iron (Fe) binuclear sites (BNSs) with two conjoint MnN₄ and FeN₄ moieties (MnFeN₈) anchored onto a graphite-like structure (GLS) (Mn-Fe BNSs/GLS) were constructed. The binuclear MnFeN₈ structure was verified experimentally and theoretically. Magnetic measurements and Gaussian calculations reveal that this unique Mn-Fe BNSs exhibit strong short-range electronic interaction between Mn and Fe sites, which decouples two paired d electrons in Fe sites, thereby transforming Fe sites from an intermediate to a high spin state. The optimal electronic configuration of Fe sites and their binuclear structure facilitate an oxygen reduction reaction (ORR) thermodynamically and dynamically, respectively, endowing Mn-Fe BNSs with improved ORR performance.

KEYWORDS

manganese (Mn)-iron (Fe) binuclear sites, synergistic effect, spin state, oxygen reduction reaction

1 Introduction

Oxygen reduction reaction (ORR) is an important cathodic reaction for fuel cells [1–5]. The widespread adoption of fuel cells is limited by the ORR process [6, 7]. To date, platinum (Pt)-based materials have been recognized as efficient catalysts for ORR. However, Pt-based catalysts account for 55% of the cost of fuel cell stacks (related to its scarcity) [8], rendering the need for meeting demands for the mass production of fuel cells problematic.

Recently, significant advances were achieved in single-atom catalysts (SACs) with singly separated transition metal atoms on nitrogen (N)-doped carbon (C)-based substrates, typically denoted as M-N_x/C catalysts [9–11]. For ORR catalysts, M-N_x/C catalysts with MN₄ structure have been systematically studied [7]. Among these MN₄ structures, the FeN₄ structure is comparable to the ORR activity with Pt/C and has been intensively investigated. Despite remarkable progress involving M-N_x/C catalysts, their catalytic properties require further improvement. Engineering the coordinative environment of metal sites is the most popular strategy for modulating the ORR activity. For example, construction of chloride perpendicularly coordinated FeN₄ sites [12], N and P dual-coordinated Fe sites were shown to be favorable for accelerating the ORR kinetic [13]; Strain can also

regulate the electronic structure of FeN₄ sites by effecting positive shifting of the 3d orbitals, which facilitates oxygen adsorption [14]. Despite significant achievements have been received in recent years, developing facile and effective strategies to regulate the electronic structure of the central metal site is still in great demand.

Electronic interaction between two metallic components, known as the synergistic effect, is a common strategy for modulating the catalytic properties of nanomaterials [15–25]. Utilizing the synergistic effect, exciting achievements for constructing dual-metal atomic pairs of M-N_x/C catalysts have consistently been developed. In the case of atomic-layer-deposited Pt-Ru dual-metal dimers, the interaction between H and Ru could be modulated by Pt through the synergetic effect, resulting in high hydrogen evolution activity [26]. Similarly, the 3d electronic orbitals of isolated Fe active site could be modulated by the adjacent Pt sites, endowing the Pt-Fe dimers with excellent ORR activity [27]. Isolated Fe and Co atoms on microporous N-doped nanocarbon also proved their synergistic effect as being positive to the ORR process [28]. Moreover, Zn/Co [29, 30], Cu/Zn [31], Co/Fe [32–34], and Fe/Ni [35, 36] dual-metal atomic pairs also exhibited a similar synergistic effect for promoting ORR activity compared with the single-metal SACs. However, the exact

Address correspondence to Qianling Zhang, zhql@szu.edu.cn; Jianhong Liu, liujh@szu.edu.cn; Xueliang Sun, xsun9@uwo.ca

electronic interaction of the synergistic effect and how it affects the catalytic performance of SACs remain ambiguous. It's necessary to reveal the specific mechanism in the synergistic effect for a better understanding of the structure–property relationship.

In this study, we synthesized dual-metal atomic pairs of Mn-Fe binuclear sites (Mn-Fe BNSs) anchored on graphite-like structure (GLS) (Mn-Fe BNSs/GLS) by facile pyrolyzing of the liquid polyacrylonitrile (LPAN) and metallic ions as precursors. The synergistic effect between Mn and Fe was interpreted as follows. Compared with Mn and Fe mononuclear site counterparts (denoted as Mn MNSs/GLS and Fe MNSs/GLS, respectively), the Mn sites polarized the neighboring Fe sites from an intermediate to a high spin state. This unique electronic interaction facilitated O₂ adsorption and charge transport, thus endowing Mn-Fe BNSs/GLS with excellent oxygen reduction activity.

2 Experimental

2.1 Chemical and electrocatalyst preparation

Mn-Fe BNSs/GLS was synthesized as follow: 1 g LPAN was dissolved in 50 mL ethanol to form a uniform solution (solution A). Additionally, 0.1 g total mass of MnCl₂·4H₂O and 0.1 g FeCl₃·6H₂O with specific molar ratios were dissolved in 50 mL ethanol to form a uniform solution (solution B). Then, solutions A and B were mixed under magnetic stirring. Subsequently, 0.5 g Ketjenblack EC-300J was added and stirred for 12 h. The above dispersion was vaped at 80 °C to form a viscous paste. The paste was placed into a muffle furnace and kept at 240 °C in the atmosphere for 6 h. Then the powder was undergone pyrolysis at 900 °C in N₂. Finally, the product was leached at 0.12 M HCl for 12 h, and dried at 80 °C. The preparation of Mn MNSs/GLS, Fe MNSs/GLS, and GLS were the same as for Mn-Fe BNSs/GLS, except that only Mn salt, Fe salt, or no Mn and Fe salt were used, respectively.

2.2 Material characterization

The morphologies of the samples were characterized by transmission electron microscope (TEM) (JEM-F200). Single atoms were investigated using probe aberration-corrected scanning transmission electron microscopy (STEM) (FEI Titan Cubed Themis G2 300) at the Electron Microscopy Center of Shenzhen University. The nitrogen adsorption–desorption isotherms were measured at 77 K with a Quantachrom NOVA 1000e system, using Barrett–Emmett–Teller calculations for the surface area. Chemical-state analysis of samples was determined by X-ray photoelectron spectroscopy (XPS) (ESCAKAB 250). All the peaks were corrected by the C 1s line at 284.8 eV as standard, followed by curve fitting and background subtraction. Chemical composition was determined by inductively coupled plasma-atomic emission spectrometry (ICP-AES) with a TJA IRIS (HR) spectrometer. The catalysts were also characterized by Raman spectroscopy (Renishaw). The X-ray absorption near-edge structure (XANES) measurements of the Mn and Fe K-edge and L-edge were performed using the hard X-ray microanalysis beamline at station 1W1B of the BSRF. Each sample spectrum was collected in a fluorescence yield using a solid-state detector.

2.3 Electrochemistry measurements

The electrochemical ORR measurements were performed using a three-electrode system. A glassy carbon rotating-disk electrode was used as the working electrode. A graphite electrode was used as the counter electrode, and a AgCl/Ag electrode was used as a reference electrode. We prepared the ink for the electrochemical measurement by mixing 7 mg of the catalysts, 200 μL deionized

water (DI) water, 750 μL ethanol, and 50 μL nafion (5% solution, Sigma-Aldrich), followed by sonication for 30 min to form a uniform mixture. Then, 10 μL of the ink was loaded onto the glassy carbon rotating-disk electrode (0.196 cm²) to prepare the working electrode. The loading of the catalyst on the working electrode was 0.35 mg·cm⁻². Cyclic voltammograms (CVs) were recorded in N₂- and O₂-saturated 0.1 M KOH solutions by cycling between 0.16 and 1.16 V vs. reversible hydrogen electrode (RHE) at a scan rate of 50 mV·s⁻¹. The ORR test was carried out at a scan rate of 2 mV·s⁻¹ rotated at 1,600 rpm.

2.4 Computational method

All calculations in this paper were carried out using the spin-polarized density functional theory (DFT) framework as implemented in the Vienna *ab initio* simulation package (VASP 4.5.1.). Projector augmented-wave (PAW) pseudo potentials were employed to describe electron–ion interactions. The Perdew–Burke–Ernzerhof (PBE) version of the generalized gradient approximation (GGA) was applied for the exchange and correlation function. The *k*-point grids were set as 7 × 7 × 1 and 17 × 17 × 17 for FeN₄, MnN₄, and FeMnN₈ structural optimization, as well as for the calculation of electronic properties, respectively. The PAW method was used in all calculations with a cut-off energy of 500 eV, and geometric optimizations were terminated when the energy and force on each ion were reduced below 10⁻⁶ eV and 0.01 eV·Å⁻¹. The valence states used were Fe-3d⁴s², Mn-3d⁵s², N-2s²2p³, O-2s²2p⁴, C-2s²2p², and H-1s¹. In the super-cell configuration, a sufficiently large vacuum slab (approximately 20 Å) was maintained, with the spin-polarized total energy calculations performed as part of the entire process. Additionally, the GGA + U method with U_{eff} = 4 and 4.5 eV for the Fe-3d and Mn-3d orbitals were used to improve the band structure and the magnetic properties of the transition metal complexes. In addition, van der Waals correction using Grimme's semi-empirical dispersion correction method (DFT-D³), as well as spin-polarized total energy calculations, was performed in the whole calculations. The d-band center was calculated using the equation below

$$\varepsilon = \frac{\int_{-\infty}^{\infty} \chi \rho(\chi) d\chi}{\int_{-\infty}^{\infty} \rho(\chi) d\chi} \quad (1)$$

Then, the Gibbs free energies for each of the ORR steps are defined as follows

$$\Delta G = \Delta E + \Delta ZPE - T\Delta S + G_{\text{pH}} + G_U \quad (2)$$

where ΔE is the reaction energy obtained from the DFT calculations; ΔZPE is the zero-point energy change, T is the temperature (298.15 K in this work), and ΔS is the entropy change. G_U is the corrected free energy of the specific electrode potential and defined as follow

$$G_U = -neU \quad (3)$$

where n is the number of electrons transferred, and U is the electrode potential; G_{pH} is the corrected free energy of the H⁺ ion concentration, and the pH is assumed to be 14 for the alkaline conditions in this work.

The free energy force field 9 (FEFF9) code calculated X-ray absorption spectra using the real-space Green's function (RSGF) formulation of the multiple-scattering theory employed in this work to simulate the K-edge XANES spectra. The FEFF program was used for *ab initio* multiple-scattering calculations of XAFS and various other spectra involving atom clusters. The FEFF code used a self-consistent DFT calculation of the Fermi energy based on the RSGF approach with muffin-tin potentials for a given lattice

structure. The treatment of X-ray absorption was then separated into atomic and scattering parts. For XANES calculation, FEFF implements the technique, which includes contributions from all orders of scattering within a cluster containing the absorber and scatters. The FEFF code also incorporates a GW-based self-energy, based on the Hedin–Lundqvist plasmon-pole model that includes the effects of electron–electron interactions. This method is well-tested and is typically a good approximation for extended X-ray absorption fine structure (EXAFS) and reasonable for XANES. Compared with the full-potential calculations, we found that the FEFF calculation of densities of states was typically in fairly good agreement with DFT for many materials. In the VASP software, the PBE and GGA functions were used as the default for all relaxation calculations. As PBE can lead to systematic errors of up to 5% in lattice parameters, we tested the sensitivity of the computed XANES spectra to $\pm 5\%$ changes in the lattice parameters.

Comsol simulation was used to estimate the impact of the micropore structure of the cathode on the current density, and the local electric field intensity surrounding the electrolyte was calculated using a finite element numerical method.

3 Results and discussions

3.1 Morphology and structure

The typical synthetic process of Mn-Fe BNSs/GLS is shown in Fig. 1(a). First, LPAN was synthesized by radical telomerization of acrylonitrile (AN) with 3-mercaptopropionic acid as a chain transfer agent [37]. As-prepared LPAN was dissolved in ethanol to form a homogeneous solution. Then, $\text{MnCl}_2 \cdot 6\text{H}_2\text{O}$ and $\text{FeCl}_3 \cdot 6\text{H}_2\text{O}$ with specific mass ratios, together with Ketjenblack EC-300J, were dissolved in the above solution. Subsequently, the above solution was vaporized in an oil bath. After pre-oxidation and

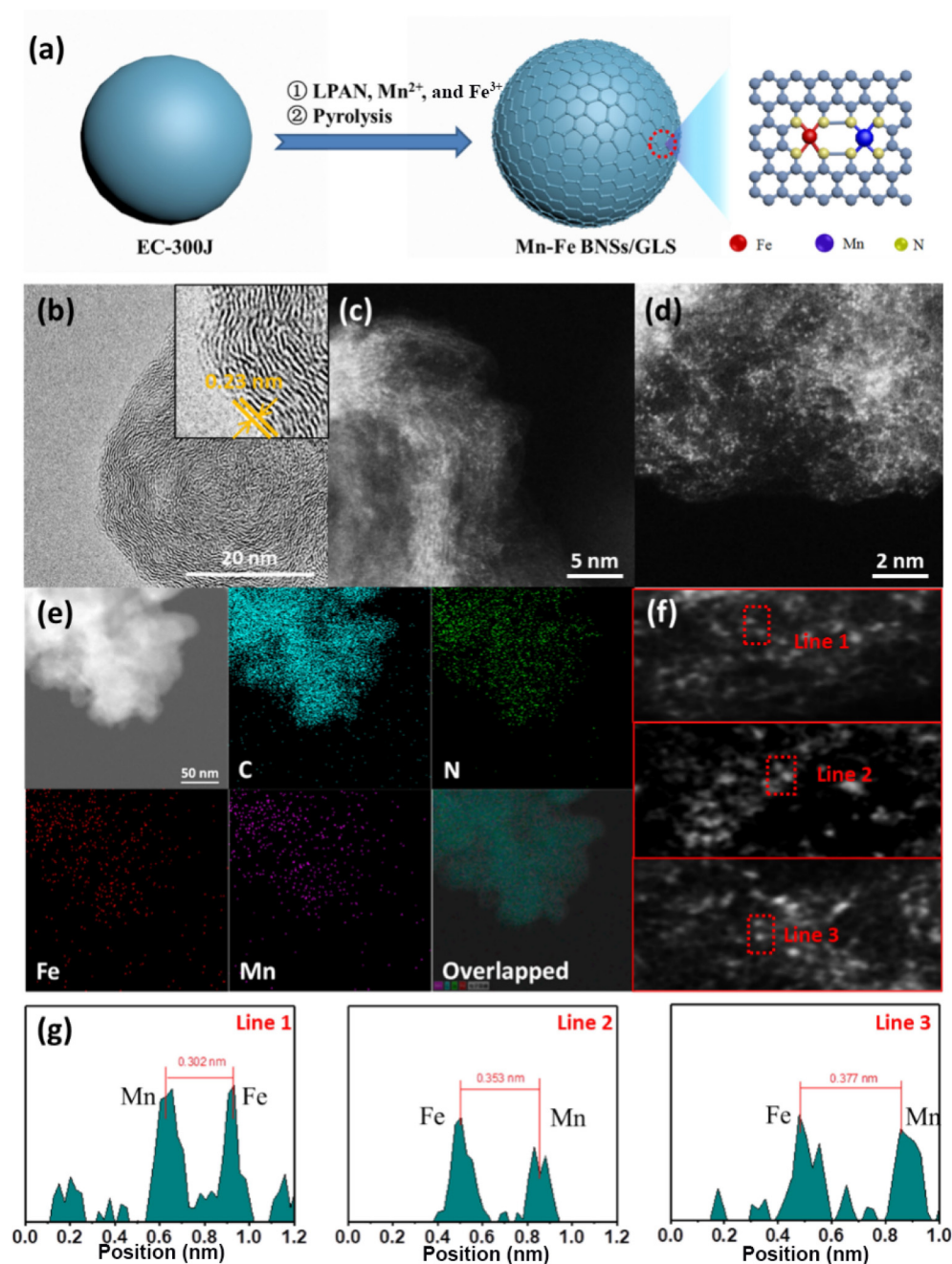


Figure 1 (a) Synthetic scheme of Mn-Fe BNSs/GLS, (b) TEM image of Mn-Fe BNSs/GLS, ((c) and (d)) AC-HAADF STEM image of Mn-Fe BNSs/GLS at different magnifications, (e) elemental mapping of C, N, Mn, and Fe in selected areas, (g) Mn-Fe binuclear sites highlighted by red squares, and (f) corresponding line-profile results.

calcination. The LPAN was carbonized to form a GLS [37–39]. Eventually, the as-prepared mixture was leached by 0.12 M hydrogen chloride (HCl) to remove superfluous metal species and Mn-Fe BNSs/GLS was synthesized. Mn MNSs/GLS and Fe MNSs/GLS as counterparts were synthesized using the same strategy.

In Fig. 1(b), the TEM image shows a sphere-like morphology with a GLS for Mn-Fe BNSs/GLS, and the lattice space is 0.23 nm, which corresponds to the (002) facet of graphite and indicates the formation of GLS. No metallic particle was observed. As shown in Figs. 1(c) and 1(d), aberration-corrected high-angle annular dark-field scanning TEM (AC-HAADF-STEM) suggests discrete bright dots anchored on the surface of the C substrate, indicating that Mn and Fe are atomically anchored onto the GLS. The elemental mapping of Mn-Fe BNSs/GLS shown in Fig. 1(e) verifies that Mn, Fe, and N are uniformly dispersed on Mn-Fe BNSs/GLS. Furthermore, dimers can be observed more clearly (Fig. 1(f)), in which Mn/Fe atomic pairs can be recognized by bright spots marked by a red square. These spots present as pairs, and the distance measurement between two atoms in the representative bright spot pairs is approximately 0.3–0.4 nm (Fig. 1(g)), such a close distance between two atomic sites may trigger a short-range electronic interaction between them (It is further explained below). Moreover, Mn MNSs/GLS and Fe MNSs/GLS exhibited similar morphology and atomic dispersion of metallic sites as shown in Figs. S3 and S4 in the Electronic Supplementary Material (ESM). The metal loading and molar ratio of Mn and Fe were measured by ICP-mass spectrometry (ICP-MS) after microwave digestion in concentrated nitrate. For Mn MNSs/GLS and Fe MNSs/GLS, the mass percentage of Mn and Fe is 0.34 wt.% and 1.19 wt.%, respectively. However, the mass percentage of Mn and Fe is 0.97 wt.% and 0.98 wt.% in Mn-Fe BNSs/GLS, respectively,

suggesting that the molar ratio of Mn and Fe is close to 1:1. The mass percentage of Mn in Mn-Fe BNSs/GLS is much higher than in Mn MNSs/GLS, despite the feeding amount of Mn in the precursor being identical. This is evidence that interaction between Mn and Fe occurs, rendering Mn and Fe in Mn-Fe BNSs/GLS likely to form binuclear dimers.

X-ray diffraction (XRD), XPS, and X-ray absorption fine structure (XAFS) were employed to further verify the above results. First, the XRD patterns suggest that all the samples without metal species (Fig. S5 in the ESM), which is in accordance with the results of TEM. The XPS results (Figs. S6–S9 in the ESM) demonstrate that N mainly exists as pyridinic N, pyrrolic N or M-N₂, graphitic N and oxidized N [40, 41], while trace Mn and Fe are also detected in Mn MNSs/GLS, Fe MNSs/GLS, and Mn-Fe BNSs/GLS. To further characterize the chemical and electronic structure of Mn-Fe BNSs/GLS, XAFS spectra were collected at station 1W1B of the Beijing Synchrotron Radiation Facility (BSRF). The XANES results of the Mn and Fe K-edge of Mn-Fe BNSs/GLS are shown in Figs. 2(a) and 2(d), respectively. The threshold energy (E_0) determined by the maximum value of the first-order derivative of the edge of the white line suggested that the valence of Mn and Fe in Mn-Fe BNSs/GLS is close to +2 and +3 respectively, which is similar to those for Mn MNSs/GLS and Fe MNSs/GLS (Figs. S10(a) and S11(a) in the ESM) [42]. EXAFS of Mn-Fe BNSs/GLS (Figs. 2(b) and 2(e)) suggest that the coordinative structures of Mn and Fe are significantly different from the metal references. Fourier transformed EXAFS (FT-EXAFS) shown in Figs. 2(c) and 2(f) verified that Mn and Fe in Mn-Fe BNSs/GLS merely deliver the first coordinative shell assigned to the M-N path. This provides evidence that Mn and Fe are anchored by N atoms on the GLS to form single atomic sites. Mn BNSs/GLS and Fe BNSs/GLS also exhibit similar results (see

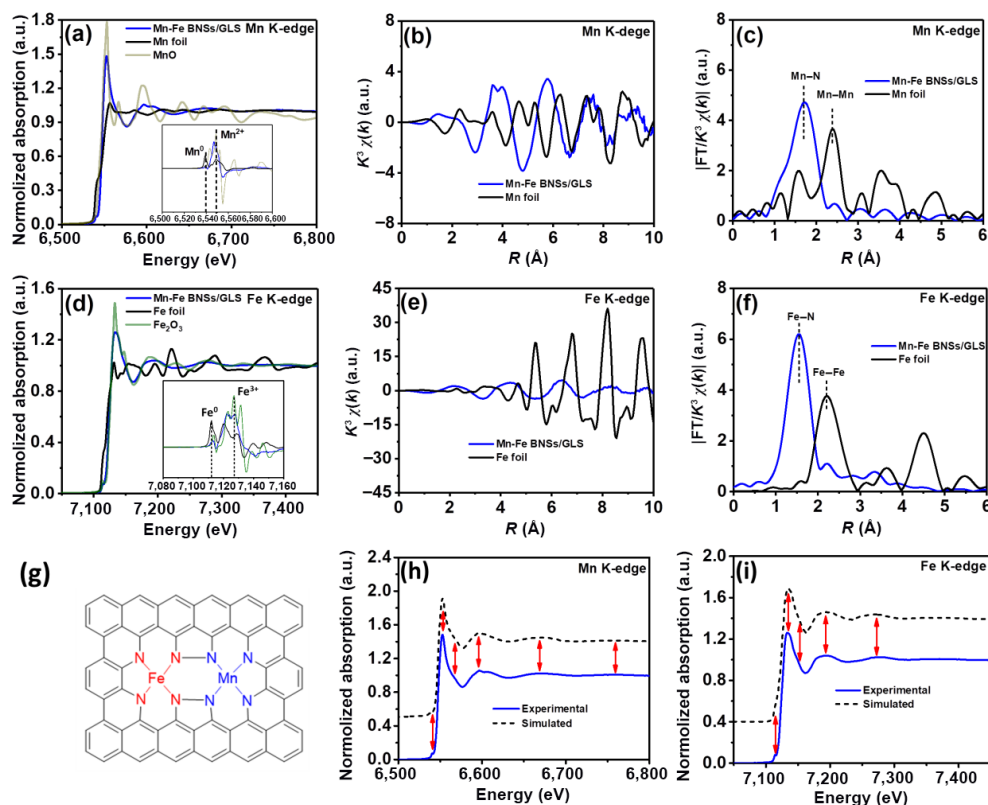


Figure 2 (a) The XANES results for the Mn K-edge of Mn-Fe BNSs/GLS, the Mn foil, and MnO. (b) EXAFS of the Mn K-edge of Mn-Fe BNSs/GLS and the Mn foil. (c) FT-EXAFS of the Mn K-edge of Mn-Fe BNSs/GLS and the Mn foil. (d) The XANES of the Fe K-edge of Mn-Fe BNSs/GLS, the Fe foil, and Fe₂O₃. (e) The EXAFS of the Mn K-edge of Mn-Fe BNSs/GLS and the Fe foil. (f) The FT-EXAFS of the Mn K-edge of Mn-Fe BNSs/GLS and the Fe foil. (g) Schematic illustration of the binuclear MnFeN₂ structure in Mn-Fe BNSs/GLS. A comparison between the XANES experimental spectrum of the (h) Mn K-edge and the (i) Fe K-edge and the theoretical spectrum calculated using the depicted structures in (g).

Figs. S10(c) and S11(c) in the ESM). The fitting of FT-EXAFS suggested coordinative numbers (CN) of Mn-N and Fe-N in Mn MNSs/GLS, Fe MNSs/GLS, and Mn-Fe BNSs/GLS are close to 4 (Figs. S10(d), S11(d), S12, and Table S1 in the ESM), implying the formation of planar MnN_4 and FeN_4 moieties in the above samples. The comparison of white-line intensities of the Mn and Fe K-edge in Fig. S13 in the ESM implies that short-range electronic interaction exists between Mn and Fe sites, and this is consistent with observations in AC-HAADF-STEM images where the distance between Mn and Fe sites is approximately 0.3–0.4 nm. This suggests that MnN_4 and FeN_4 formed dimers for planar MnFeN_8 moiety (see Fig. 2(g)). Furthermore, the theoretical XANES spectra, calculated based on the MnFeN_8 moiety shown in Fig. 2(g), excellently match with the experimental spectra (Figs. 2(h) and 2(i)), indicating the possible structure of Mn-Fe BNSs with MnFeN_8 moiety.

The different ^{57}Fe Mössbauer spectroscopic characterizations between Fe MNSs/GLS and Mn-Fe BNSs/GLS (Fig. S14 and Table S2 in the ESM) imply that the short-range electronic interaction between Mn and Fe atomic sites varied the spin state of Fe in MnFeN_8 moiety. Zero-field cooling (ZFC) temperature dependence inverse susceptibilities were employed to analyze the spin state of Mn and Fe sites experimentally. Using the M - T curves (Fig. 3(a)), Langevin theory and the Curie-Weiss law, the number of unpaired electrons of MnN_4 and FeN_4 could be calculated [43], and detailed process of calculations is shown in the ESM. For Mn MNSs/GLS and Fe MNSs/GLS, the number of unpaired electrons of MnN_4 and FeN_4 is determined as ~ 5 and ~ 3 , thus Mn^{II} and Fe^{III} are in a high spin state and intermediate spin state, respectively. For Mn-Fe BNSs/GLS, both numbers of unpaired electrons in Mn and Fe sites are ~ 5 , suggesting that when FeN_4 coupled with MnN_4 , Fe^{III} in FeN_4 is transformed from an intermediate to high spin state. Gaussian calculation was used to further illuminate the electronic configuration of Fe. The calculation models are shown in Fig. 3(b) and Fig. S15 in the ESM. The calculated effective magnetic moments of Fe (Fig. S16 in the ESM) are similar to the result of the M - T curves, and the 3d electronic configurations of Fe in Fe MNSs/GLS and Mn-Fe BNSs/GLS are determined as $(d_{xy})^2(d_{yz})^1(d_{xz})^1(d_{x^2-y^2})^1(d_{z^2})^0$ (intermediate spin state) and $(d_{xy})^1(d_{yz})^1(d_{xz})^1(d_{x^2-y^2})^1(d_{z^2})^1$ (high spin state) (see Fig. 3(c)), respectively. This suggests that a pair of

electrons in the d_{xy} orbital of Fe have been decoupled, and one electron has been excited to the d_{z^2} orbital to form Fe^{III} with a high spin state. To further explain this phenomenon, we analyzed the d orbital configurations of Mn and Fe. The orientation of the five d orbitals is shown in Fig. 3(b). It is shown that the d orbitals between Mn and Fe sites are able to form σ -, π -, and δ - bonds, respectively (Fig. 3(d)). When a pair of electrons in the Fe d_{xy} orbital is decoupled and one has been excited to the d_{z^2} orbital, all the d orbitals in both Mn and Fe become half-filled (Fig. 3(d)); this is an energetically preferred state according to the Hund rule and Pauli exclusion principle, and, as such, represents a reasonable result.

The N isothermal desorption isotherms of Mn-Fe BNSs/GLS, Mn MNSs/GLS, Fe MNSs/GLS, and GLS in Figs. S17 and S18 in the ESM suggest the porous characteristics of these catalysts. Comsol simulation suggests that the porous structure locally enhances the electrostatic field and concentrates the free electron density (Figs. S19–S21 in the ESM), thus further contributes to the increase in the catalytic current density.

3.2 Electrochemical study

The catalytic activities of the as-prepared Mn-Fe BNSs/GLS for ORR are evaluated in a 0.1 M potassium hydroxide (KOH) solution by rotating disc electrode (RDE), and commercial 20 wt.% Pt/C is used as a reference (Fig. S22 in the ESM). As shown in the linear sweep voltammetry (LSV) results (Fig. 4(a)), Mn-Fe BNSs/GLS achieves the highest ORR activity, with the highest onset potential and half-wave potential ($E_{1/2}$) of 0.918 V (vs. RHE), superior to that of Fe MNSs/GLS (0.869 V) and Mn MNSs/GLS (0.882 V), and 77 mV more positive than that of commercial Pt/C (0.841 V). The limiting diffusion current density (J_L) of Mn-Fe BNSs/GLS reaches 6.05 $\text{mA}\cdot\text{cm}^{-2}$, better than that of Fe MNSs/GLS ($J_L = 5.43 \text{ mA}\cdot\text{cm}^{-2}$), Mn MNSs/GLS ($J_L = 4.62 \text{ mA}\cdot\text{cm}^{-2}$), and Pt/C ($J_L = 5.49 \text{ mA}\cdot\text{cm}^{-2}$). As shown in Fig. 4(b), the Tafel slope of Mn-Fe BNSs/GLS is 76.63 $\text{mV}\cdot\text{dec}^{-1}$, which is lower than that of Fe MNSs/GLS (89.70 $\text{mV}\cdot\text{dec}^{-1}$), Mn MNSs/GLS (94.37 $\text{mV}\cdot\text{dec}^{-1}$), and Pt/C (78.28 $\text{mV}\cdot\text{dec}^{-1}$), indicating the fastest reactive kinetics for Mn-Fe BNSs/GLS. When the current density is normalized to the mass of metal, the current density of Mn-Fe BNSs/GLS is much better than that of Pt/C (Fig. 4(c)), suggesting the advantage of ultra-low metal-loading, ultra-

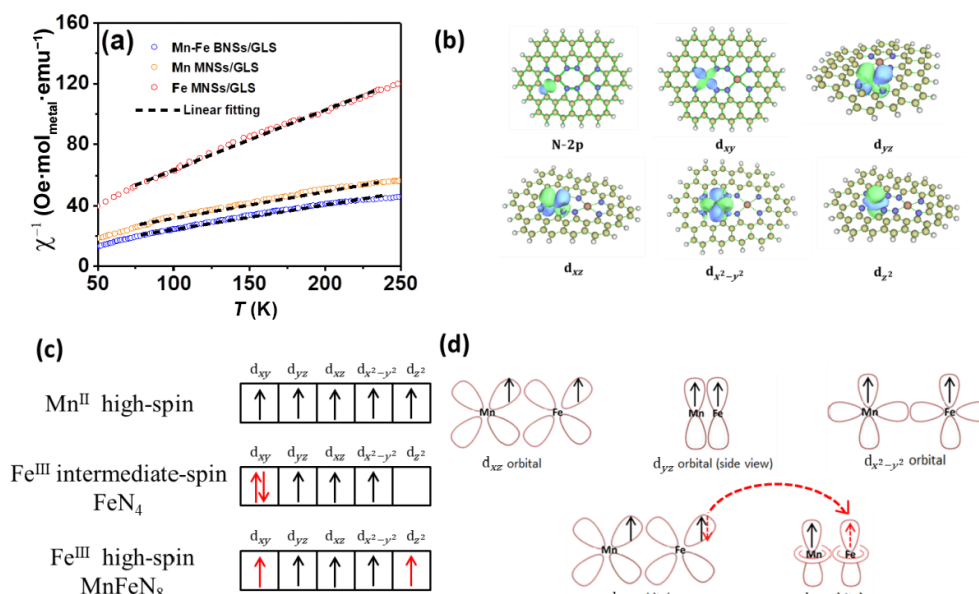


Figure 3 (a) Temperature dependence inverse susceptibilities of Mn MNSs/GLS, Fe MNSs/GLS, and Mn-Fe BNSs/GLS. (b) The calculation models and valence electron orbitals of MnFeN_8 , (c) d electron orbital configurations of Mn^{II} with a high spin state and Fe^{III} with an intermediate spin state and high spin state, and (d) d-d interaction between Mn and Fe in Mn-Fe BNSs/GLS.

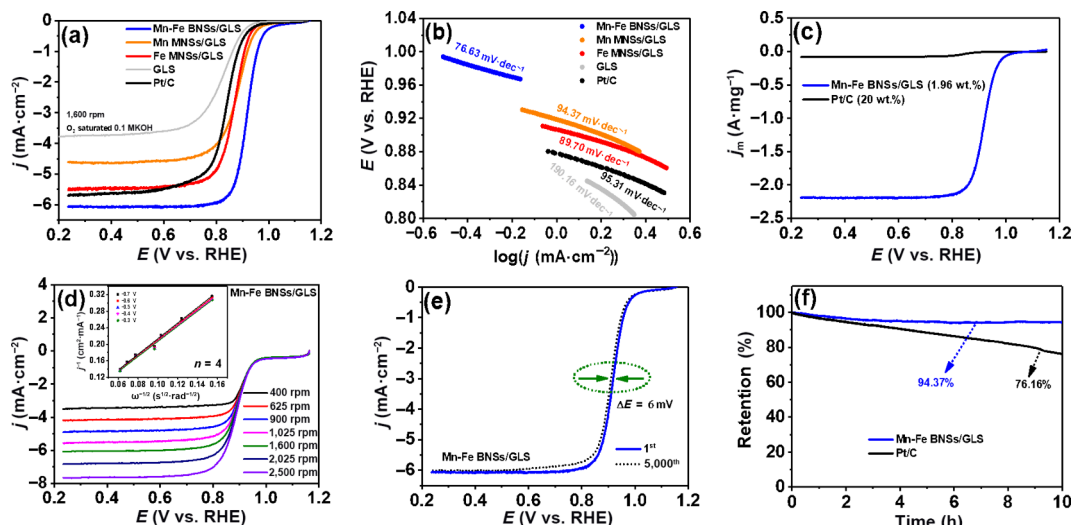


Figure 4 (a) The LSV curves and (b) Tafel plots of Mn-Fe BNSs/GLS, Mn MNSs/GLS, Fe MNSs/GLS, GLS, and commercial Pt/C at a rotation speed of 1,600 rpm. (c) LSV curves of Mn-Fe BNSs/GLS and Pt/C with current density normalized to the mass of metal. (d) LSV curves of Mn-Fe BNSs/GLS before and after 5,000 CVs. (e) I - t curves of Mn-Fe BNSs/GLS and Pt/C at 0.8 V. All electrochemical data were performed in an O_2 -saturated 0.1 M KOH solution at a scan rate of $5 \text{ mV} \cdot \text{s}^{-1}$.

high dispersion, and the use of active sites. The improved ORR activity of Mn-Fe BNSs/GLS compared with Fe MNSs/GLS and Mn MNSs/GLS verifies that the strong electronic interaction between Mn and Fe sites, the so-called synergetic effect, greatly enhanced ORR activity, and enlarged electrochemical active area (ECA) (Fig. S23 in the ESM). Moreover, the ORR activity of samples with different Mn and Fe suggests that the sample with Mn:Fe = 1:1 exhibits the best ORR activity, suggesting that Mn and Fe become dimers that benefited the ORR process (Fig. S24 in the ESM). The improved ORR activity of Mn-Fe BNSs/GLS compared with state-of-the-art non-noble metal catalysts (Table S3 in the ESM) emphasizes the advancements of the as-prepared Mn-Fe BNSs/GLS. As presented in Fig. 3(d), Koutecky–Levich plots of Mn-Fe BNSs/GLS verify that the value of the electron transfer number (n) is 4.0, which is similar to those of Mn MNSs/GLS, Fe MNSs/GLS, and Pt/C (Fig. S25 in the ESM). This indicates that oxygen reduction via a direct four-electron pathway in an alkaline medium, alongside H_2O , is the final product [42–44].

The durability of Mn-Fe BNSs/GLS was evaluated. As shown in Figs. 4(e) and 4(f) and Fig. S26 in the ESM, continuous cyclic and chronoamperometric (CA) curves demonstrate that Mn-Fe BNSs/GLS exhibits negligible activity attenuation, while Pt/C appears to indicate a serious recession. The TEM image of Mn-Fe BNSs/GLS after the durability test suggests that the single atomic sites survived (Fig. S27 in the ESM). This excellent stability can be attributed to the strong interaction between metallic sites and the GLS, which was confirmed by the soft XAFS shown in Fig. S28 in the ESM.

Based on above advantages, Mn-Fe BNSs/GLS was used as a catalyst for the cathode of a zinc-air battery (ZAB). As depicted in Fig. S29 and Table S4 in the ESM, the primary ZAB based on the Mn-Fe BNSs/GLS exhibits an impressive open-circuit voltage of 1.525 V, and offers a peak power density of approximately $118.1 \text{ mW} \cdot \text{cm}^{-2}$, high specific capacity of $821.3 \text{ mAh} \cdot \text{g}_{\text{Zn}}^{-1}$, and excellent discharge stabilities. The above results suggest that Mn-Fe BNSs/GLS has significant potential for application in ZABs.

3.3 Theoretical study

To further understand the ORR reaction process, DFT calculations were conducted to study the active sites and the reaction mechanism. For MnFeN₈, DFT calculation revealed that all oxygen-contained intermediates preferred to adsorb onto the

Fe site; therefore, the Fe site should be the active site. The elementary reaction pathways of MnN₄, FeN₄, and MnFeN₈ moieties are shown in Figs. 5(a)–5(c), respectively. The free energy diagram of MnN₄, FeN₄, and MnFeN₈ moieties are shown in Figs. 5(d)–5(f). Herein, MnFeN₈ and FeN₄ for which the rate determining step (RDS) is *OOH formation step with the lowest barrier value in case of 1.23 V output potential, that is, zero overpotential (Figs. 5(d) and 5(f)). For MnN₄, the RDS is desorption of *OH at 1.23 V (Fig. 5(e)). The free energy barrier of RDS for MnN₄, FeN₄, and MnFeN₈ was calculated as 0.41, 0.39, and 0.32 eV, respectively. According to the above results, the potential of thermodynamic spontaneous ORR for MnFeN₈ was calculated as 0.92 V, which is higher than that of MnN₄ (0.82 V) and FeN₄ (0.84 V). The activation energies for *OOH dissociation is a crucial and dynamic step for breaking the O–O bond for the 4e[−] ORR associative pathway [44]. For MnFeN₈, DFT calculation revealed that *OOH was adsorbed on the Fe site in the initial state (IS); then, the *OOH was dissociated to form *O and *OH and was adsorbed on Fe and Mn sites, respectively, in the final state (FS), as depicted in Fig. 5(g). For MnN₄ and FeN₄, *OOH was adsorbed on the catalytically active metallic site in the IS. In the FS, *O and *OH were adsorbed on the metallic site and the adjacent C atom, respectively (Figs. 5(h) and 5(i)). The reaction process from the IS to the FS requires passing through a transition state (TS) and overcoming an energy barrier. However, the TS energy barrier of MnFeN₈ is as low as 0.27 eV (Fig. 5(g)), which is much lower than that of MnN₄ (0.74 eV, Fig. 5(h)) and FeN₄ (0.68 eV, Fig. 5(i)). Such a sharp drop in activation energy for breaking the O–O bond on MnFeN₈ can be attributed to Mn as a second site for adsorbing the dissociated *OH, which will promote breaking of the O–O bond and kinetically accelerate the ORR process.

Furthermore, 3d_{z²} orbital is perpendicularly situated to the MN₄ plane, and, thus, directly interacts with the 2p orbital of oxygen-contained intermediates. According to the Sabatier principle, the electronic structure of Fe 3d with a half-empty 3d_{z²} orbital is required to bind oxygen with optimal strength [45, 46]. Therefore, the high spin state of Fe in Mn-Fe BNSs/GLS matches this requirement (Fig. 3(c)). The O₂ molecular with ground-state is a spin-triplet with two unpaired electrons (Fig. S30 in the ESM). The spin-polarized Fe sites in Mn-Fe BNSs/GLS can more easily capture the O₂ molecule because of the higher bond order that is resulted from the spin–orbital interactions between Fe site with high spin and O₂ [47]. Furthermore, the high spin state of Fe sites

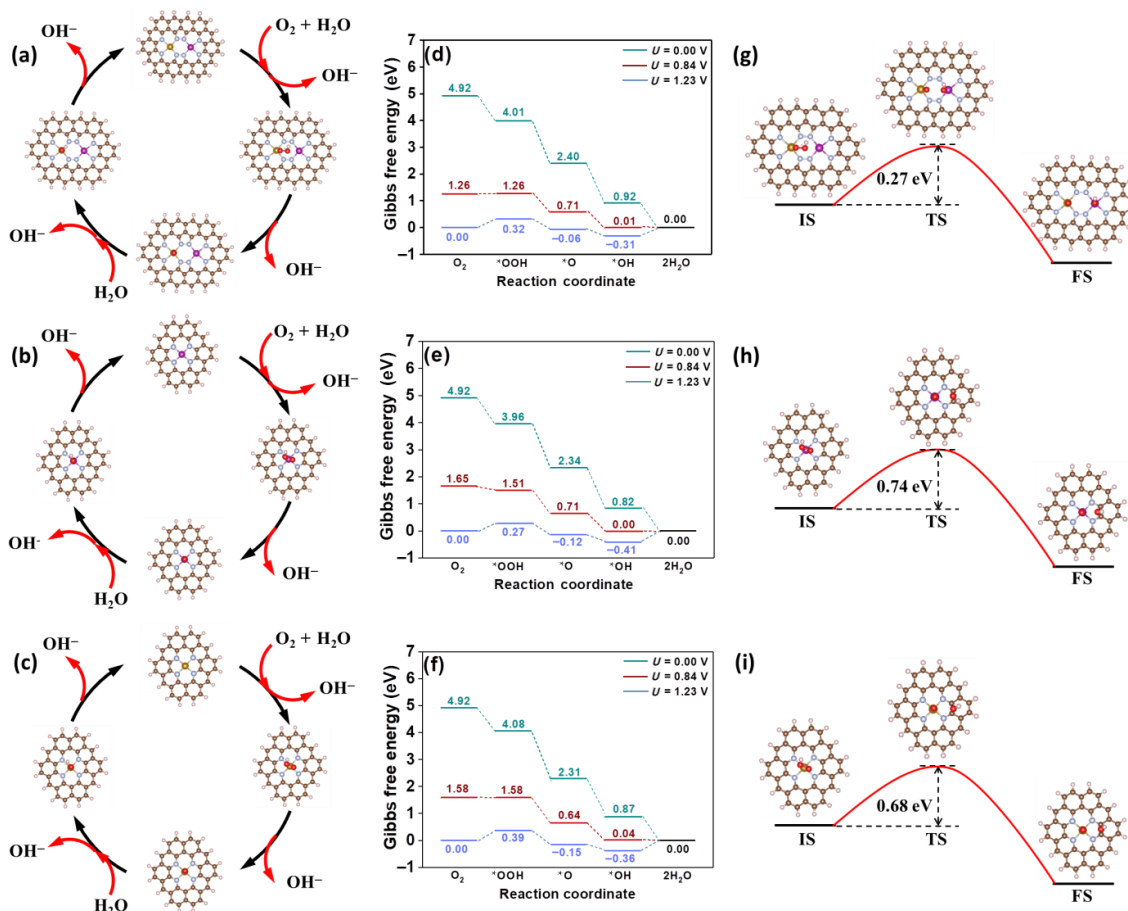


Figure 5 Reactive processes of ORR for (a) MnFeN₈, (b) MnN₄, and (c) FeN₄ moiety. Free energy diagrams of ORR for (d) MnFeN₈, (e) MnN₄, and (f) FeN₄ moiety. The reactive processes for the cleavage of O–O bond in *OOH and the corresponding kinetic barriers of (g) MnFeN₈, (h) MnN₄, and (i) FeN₄ moiety.

can also create a wider spin-related channel, which promotes charge transport during ORR [47].

4 Conclusion

In summary, we constructed dual-metal atomic pairs of Mn-Fe BNSs (MnFeN₈ moiety) on a GLS (Mn-Fe BNSs/GLS) using a facile pyrolysis strategy. The synergistic effect between Mn and Fe sites was confirmed and mainly clarified as follows: 1) the short-range electronic interaction between Mn and Fe sites rendered Fe sites were transformed from an intermediate to a high spin state; 2) the polarized Fe site presents optimal electronic configuration for the adsorption of spin-triplet O₂ and oxygen-containing intermediates, which benefits the ORR process; 3) the Mn-Fe BNSs structure optimizes the free energy of ORR and facilitates the cleavage of O–O bond in O₂. The above advantages can greatly improve ORR activity. This work represents a new class of dual atomic sites catalysts for both fundamental research and practical applications.

Acknowledgements

We appreciate the financial support of Shenzhen Basic Research Project (Nos. JCYJ20170818092720054, JCYJ20190808145203535, and JCYJ20190808144413257), National Natural Science Foundation of China (No. 21671136), Postdoctoral Science Foundation of China (No. 2019M663085), Major Programs for Science and Technology Development of Shenzhen (Nos. JSGG20160328151657828 and XCL201110060), Major Industrial Projects of Shenzhen (No. s2017001850011), and the Project of Natural Science Foundation of Guangdong Province (Nos. 2020A1515010380 and 2014A030311028). We thank the Electron

Microscopy Center at Shenzhen University for AC HAADF-STEM characterization and Instrumental Analysis Center at Shenzhen University (Xili Campus) for providing different facilities for material analysis. We are also grateful to Zhengzhou MiCe Information Technology Co., Ltd., and Huasuan Technology Co., Ltd. for providing the ZFC temperature dependence inverse susceptibilities test and theoretical calculation, respectively.

Electronic Supplementary Material: Supplementary material (experimental details, Figs. S1–S30 and Tables S1–S4 in the ESM) is available in the online version of this article at <https://doi.org/10.1007/s12274-022-4979-x>.

References

- Guo, D. H.; Shibuya, R.; Akiba, C.; Saji, S.; Kondo, T.; Nakamura, J. Active sites of nitrogen-doped carbon materials for oxygen reduction reaction clarified using model catalysts. *Science* **2016**, *351*, 361–365.
- Chen, K. J.; Liu, K.; An, P. D.; Li, H. J. W.; Lin, Y. Y.; Hu, J. H.; Jia, C. K.; Fu, J. W.; Li, H. M.; Liu, H. et al. Iron phthalocyanine with coordination induced electronic localization to boost oxygen reduction reaction. *Nat. Commun.* **2020**, *11*, 4173.
- Li, Y. G.; Dai, H. J. Recent advances in zinc-air batteries. *Chem. Soc. Rev.* **2014**, *43*, 5257–5275.
- Zhao, C. X.; Liu, J. N.; Wang, J.; Ren, D.; Li, B. Q.; Zhang, Q. Recent advances of noble-metal-free bifunctional oxygen reduction and evolution electrocatalysts. *Chem. Soc. Rev.* **2021**, *50*, 7745–7778.
- Liu, Z. Y.; Zhao, Z. P.; Peng, B. S.; Duan, X. F.; Huang, Y. Beyond extended surfaces: Understanding the oxygen reduction reaction on nanocatalysts. *J. Am. Chem. Soc.* **2020**, *142*, 17812–17827.

- [6] Chattot, R.; Le Bacq, O.; Beermann, V.; Kühn, S.; Herranz, J.; Henning, S.; Kühn, L.; Asset, T.; Guétaz, L.; Renou, G. et al. Surface distortion as a unifying concept and descriptor in oxygen reduction reaction electrocatalysis. *Nat. Mater.* **2018**, *17*, 827–833.
- [7] Ma, Q. L.; Jin, H. H.; Zhu, J. W.; Li, Z. L.; Xu, H. W.; Liu, B. S.; Zhang, Z. W.; Ma, J. J.; Mu, S. C. Stabilizing Fe-N-C catalysts as model for oxygen reduction reaction. *Adv. Sci.* **2021**, *8*, 2102209.
- [8] Gao, R. J.; Wang, J.; Huang, Z. F.; Zhang, R. R.; Wang, W.; Pan, L.; Zhang, J. F.; Zhu, W. K.; Zhang, X. W.; Shi, C. X. et al. Pt/Fe₂O₃ with Pt-Fe pair sites as a catalyst for oxygen reduction with ultralow Pt loading. *Nat. Energy* **2021**, *6*, 614–623.
- [9] Song, Z. X.; Zhang, L.; Doyle-Davis, K.; Fu, X. Z.; Luo, J. L.; Sun, X. L. Recent advances in MOF-derived single atom catalysts for electrochemical applications. *Adv. Energy Mater.* **2020**, *10*, 2001561.
- [10] Wan, C. Z.; Duan, X. F.; Huang, Y. Molecular design of single-atom catalysts for oxygen reduction reaction. *Adv. Energy Mater.* **2020**, *10*, 1903815.
- [11] Yu, Y.; Zhang, J. N. Optimizing configuration engineering of edge-hosted Fe-N_x active sites for oxygen reduction reaction. *Chem. Catal.* **2021**, *1*, 1155–1157.
- [12] Han, Y. H.; Wang, Y. G.; Xu, R. R.; Chen, W. X.; Zheng, L. R.; Han, A. J.; Zhu, Y. Q.; Zhang, J.; Zhang, H. B.; Luo, J. et al. Electronic structure engineering to boost oxygen reduction activity by controlling the coordination of the central metal. *Energy Environ. Sci.* **2018**, *11*, 2348–2352.
- [13] Yuan, K.; Lützenkirchen-Hecht, D.; Li, L. B.; Shuai, L.; Li, Y. Z.; Cao, R.; Qiu, M.; Zhuang, X. D.; Leung, M. K. H.; Chen, Y. W. et al. Boosting oxygen reduction of single iron active sites via geometric and electronic engineering: Nitrogen and phosphorus dual coordination. *J. Am. Chem. Soc.* **2020**, *142*, 2404–2412.
- [14] Li, J. Z.; Zhang, H. G.; Samarakoon, W.; Shan, W. T.; Cullen, D. A.; Karakalos, S.; Chen, M. J.; Gu, D. M.; More, K. L.; Wang, G. F. et al. Thermally driven structure and performance evolution of atomically dispersed FeN₄ sites for oxygen reduction. *Angew. Chem., Int. Ed.* **2019**, *58*, 18971–18980.
- [15] Zhang, Y.; Huang, B. L.; Luo, G.; Sun, T.; Feng, Y. G.; Wang, Y. C.; Ma, Y. H.; Shao, Q.; Li, Y. F.; Zhou, Z. Y. et al. Atomically deviated Pd-Te nanoplates boost methanol-tolerant fuel cells. *Sci. Adv.* **2020**, *6*, eaba9731.
- [16] Lyu, X.; Jia, Y.; Mao, X.; Li, D. H.; Li, G.; Zhuang, L. Z.; Wang, X.; Yang, D. J.; Wang, Q.; Du, A. J. et al. Gradient-concentration design of stable core-shell nanostructure for acidic oxygen reduction electrocatalysis. *Adv. Mater.* **2020**, *32*, 2003493.
- [17] Li, H. G.; Di, S. L.; Niu, P.; Wang, S. L.; Wang, J.; Li, L. A durable half-metallic diatomic catalyst for efficient oxygen reduction. *Energy Environ. Sci.* **2022**, *15*, 1601–1610.
- [18] Alkhalifah, M. A.; Howchen, B.; Staddon, J.; Celorrio, V.; Tiwari, D.; Fermin, D. J. Correlating orbital composition and activity of LaMn_xNi_{1-x}O₃ nanostructures toward oxygen electrocatalysis. *J. Am. Chem. Soc.* **2022**, *144*, 4439–4447.
- [19] Zhu, G. H.; Yang, H. Y.; Jiang, Y.; Sun, Z. Q.; Li, X. P.; Yang, J. P.; Wang, H. F.; Zou, R. J.; Jiang, W.; Qiu, P. P. et al. Modulating the electronic structure of FeCo nanoparticles in N-doped mesoporous carbon for efficient oxygen reduction reaction. *Adv. Sci.* **2022**, *9*, 2200394.
- [20] Li, R. Z.; Wang, D. S. Understanding the structure–performance relationship of active sites at atomic scale. *Nano Res.* **2022**, *15*, 6888–6923.
- [21] Cui, T. T.; Wang, Y. P.; Ye, T.; Wu, J.; Chen, Z. Q.; Li, J.; Lei, Y. P.; Wang, D. S.; Li, Y. D. Engineering dual single-atom sites on 2D ultrathin N-doped carbon nanosheets attaining ultra-low-temperature zinc-air battery. *Angew. Chem., Int. Ed.* **2022**, *61*, e202115219.
- [22] Zheng, X. B.; Li, B. B.; Wang, Q. S.; Wang, D. S.; Li, Y. D. Emerging low-nuclearity supported metal catalysts with atomic level precision for efficient heterogeneous catalysis. *Nano Res.* **2022**, *15*, 7806–7839.
- [23] Chao, G. J.; An, X. Y.; Zhang, L. S.; Tian, J.; Fan, W.; Liu, T. X. Electron-rich platinum electrocatalysts supported onto tin oxides for efficient oxygen reduction. *Compos. Commun.* **2021**, *24*, 100603.
- [24] Zhu, T. Y.; Feng, Q. C.; Liu, S. L.; Zhang, C. Metallogel-derived 3D porous carbon nanosheet composites as an electrocatalyst for oxygen reduction reaction. *Compos. Commun.* **2020**, *20*, 100376.
- [25] Hu, J.; Cao, L. J.; Wang, Z.; Liu, J. L.; Zhang, J. J.; Cao, Y. L.; Lu, Z. G.; Cheng, H. Hollow high-entropy metal organic framework derived nanocomposite as efficient electrocatalyst for oxygen reduction reaction. *Compos. Commun.* **2021**, *27*, 100866.
- [26] Zhang, L.; Si, R. R.; Liu, H. S.; Chen, N.; Wang, Q.; Adair, K.; Wang, Z. Q.; Chen, J. T.; Song, Z. X.; Li, J. J. et al. Atomic layer deposited Pt-Ru dual-metal dimers and identifying their active sites for hydrogen evolution reaction. *Nat. Commun.* **2019**, *10*, 4936.
- [27] Han, A. L.; Wang, X. J.; Tang, K.; Zhang, Z. D.; Ye, C. L.; Kong, K. J.; Hu, H. B.; Zheng, L. R.; Jiang, P.; Zhao, C. X. et al. An adjacent atomic platinum site enables single-atom iron with high oxygen reduction reaction performance. *Angew. Chem., Int. Ed.* **2021**, *60*, 19262–19271.
- [28] Wang, J.; Huang, Z. Q.; Liu, W.; Chang, C. R.; Tang, H. L.; Li, Z. J.; Chen, W. X.; Jia, C. J.; Yao, T.; Wei, S. Q. et al. Design of N-coordinated dual-metal sites: A stable and active Pt-free catalyst for acidic oxygen reduction reaction. *J. Am. Chem. Soc.* **2017**, *139*, 17281–17284.
- [29] Lu, Z. Y.; Wang, B.; Hu, Y. F.; Liu, W.; Zhao, Y. F.; Yang, R. O.; Li, Z. P.; Luo, J.; Chi, B.; Jiang, Z. et al. An isolated zinc-cobalt atomic pair for highly active and durable oxygen reduction. *Angew. Chem., Int. Ed.* **2019**, *58*, 2622–2626.
- [30] Zhu, W. J.; Zhang, L.; Liu, S. H.; Li, A.; Yuan, X. T.; Hu, C. L.; Zhang, G.; Deng, W. Y.; Zang, K. T.; Luo, J. et al. Enhanced CO₂ electroreduction on neighboring Zn/Co monomers by electronic effect. *Angew. Chem., Int. Ed.* **2020**, *59*, 12664–12668.
- [31] Deng, D. J.; Qian, J. C.; Liu, X. Z.; Li, H. P.; Su, D.; Li, H. N.; Li, H. M.; Xu, L. Non-covalent interaction of atomically dispersed Cu and Zn pair sites for efficient oxygen reduction reaction. *Adv. Funct. Mater.* **2022**, *32*, 2203471.
- [32] Bai, L. C.; Hsu, C. S.; Alexander, D. T. L.; Chen, H. M.; Hu, X. L. A cobalt-iron double-atom catalyst for the oxygen evolution reaction. *J. Am. Chem. Soc.* **2019**, *141*, 14190–14199.
- [33] Yin, S. H.; Yang, J.; Han, Y.; Li, G.; Wan, L. Y.; Chen, Y. H.; Chen, C.; Qu, X. M.; Jiang, Y. X.; Sun, S. G. Construction of highly active metal-containing nanoparticles and FeCo-N₄ composite sites for the acidic oxygen reduction reaction. *Angew. Chem., Int. Ed.* **2020**, *59*, 21976–21979.
- [34] He, Y. T.; Yang, X. X.; Li, Y. S.; Liu, L. T.; Guo, S. W.; Shu, C. Y.; Liu, F.; Liu, Y. N.; Tan, Q.; Wu, G. Atomically dispersed Fe-Co dual metal sites as bifunctional oxygen electrocatalysts for rechargeable and flexible Zn-air batteries. *ACS Catal.* **2022**, *12*, 1216–1227.
- [35] Chen, J. Y.; Li, H.; Fan, C.; Meng, Q. W.; Tang, Y. W.; Qiu, X. Y.; Fu, G. T.; Ma, T. Y. Dual single-atomic Ni-N₄ and Fe-N₄ sites constructing janus hollow graphene for selective oxygen electrocatalysis. *Adv. Mater.* **2020**, *32*, 2003134.
- [36] Wan, W. C.; Zhao, Y. G.; Wei, S. Q.; Triana, C. A.; Li, J. G.; Arcifa, A.; Allen, C. S.; Cao, R.; Patzke, G. R. Mechanistic insight into the active centers of single/dual-atom Ni/Fe-based oxygen electrocatalysts. *Nat. Commun.* **2021**, *12*, 5589.
- [37] Chang, Y. Q.; Hong, F.; He, C. X.; Zhang, Q. L.; Liu, J. H. Nitrogen and sulfur dual-doped non-noble catalyst using fluidic acrylonitrile telomer as precursor for efficient oxygen reduction. *Adv. Mater.* **2013**, *25*, 4794–4799.
- [38] Mi, H. W.; Li, Y. L.; Zhu, P. Y.; Chai, X. Y.; Sun, L. N.; Zhuo, H. T.; Zhang, Q. L.; He, C. X.; Liu, J. H. In situ coating of nitrogen-doped graphene-like nanosheets on silicon as a stable anode for high-performance lithium-ion batteries. *J. Mater. Chem. A* **2014**, *2*, 11254–11260.
- [39] Rahaman, M. S. A.; Ismail, A. F.; Mustafa, A. A review of heat treatment on polyacrylonitrile fiber. *Polym. Degrad. Stab.* **2007**, *92*, 1421–1432.
- [40] Yan, H. J.; Xie, Y.; Jiao, Y. Q.; Wu, A. P.; Tian, C. G.; Zhang, X. M.; Wang, L.; Fu, H. G. Holey reduced graphene oxide coupled with an Mo₂N-Mo₂C heterojunction for efficient hydrogen evolution. *Adv. Mater.* **2018**, *30*, 1704156.

- [41] Ye, S. H.; Luo, F. Y.; Xu, T. T.; Zhang, P. Y.; Shi, H. D.; Qin, S. Q.; Wu, J. P.; He, C. X.; Ouyang, X. P.; Zhang, Q. L. et al. Boosting the alkaline hydrogen evolution of Ru nanoclusters anchored on B/N-doped graphene by accelerating water dissociation. *Nano Energy* **2020**, *68*, 104301.
- [42] Fei, H. L.; Dong, J. C.; Feng, Y. X.; Allen, C. S.; Wan, C. Z.; Voloskiy, B.; Li, F. M.; Zhao, Z. P.; Wang, Y. L.; Sun, H. T. et al. General synthesis and definitive structural identification of MN_4C_4 single-atom catalysts with tunable electrocatalytic activities. *Nat. Catal.* **2018**, *1*, 63–72.
- [43] Shen, G. Q.; Zhang, R. R.; Pan, L.; Hou, F.; Zhao, Y. J.; Shen, Z. Y.; Mi, W. B.; Shi, C. X.; Wang, Q. F.; Zhang, X. W. et al. Regulating the spin state of Fe^{III} by atomically anchoring on ultrathin titanium dioxide for efficient oxygen evolution electrocatalysis. *Angew. Chem., Int. Ed.* **2020**, *59*, 2313–2317.
- [44] Li, J. Z.; Chen, M. J.; Cullen, D. A.; Hwang, S.; Wang, M. Y.; Li, B. Y.; Liu, K. X.; Karakalos, S.; Lucero, M.; Zhang, H. G. et al. Atomically dispersed manganese catalysts for oxygen reduction in proton-exchange membrane fuel cells. *Nat. Catal.* **2018**, *1*, 935–945.
- [45] Kramm, U. I.; Herranz, J.; Larouche, N.; Arruda, T. M.; Lefèvre, M.; Jaouen, F.; Bogdanoff, P.; Fiechter, S.; Abs-Wurmbach, I.; Mukerjee, S. et al. Structure of the catalytic sites in Fe/N/C-catalysts for O_2 -reduction in PEM fuel cells. *Phys. Chem. Chem. Phys.* **2012**, *14*, 11673–11688.
- [46] Lu, Y.; Li, L.; Zhang, Q.; Niu, Z. Q.; Chen, J. Electrolyte and interface engineering for solid-state sodium batteries. *Joule* **2018**, *2*, 1747–1770.
- [47] Sun, Y. M.; Sun, S. N.; Yang, H. T.; Xi, S. B.; Gracia, J.; Xu, Z. J. Spin-related electron transfer and orbital interactions in oxygen electrocatalysis. *Adv. Mater.* **2020**, *32*, 2003297.